Title

Monolithic nanoporous alumina membranes for ultrafiltration applications: characterization, selectivity-permeability analysis and fouling studies

Authors

Kah Peng Lee and Davide Mattia*

* corresponding author

Affiliation for all authors

Department of Chemical Engineering,
University of Bath,
Claverton Down,
Bath,
BA2 7AY, UK.

Email: D.Mattia@bath.ac.uk
Tel : +44 1225 383961
Fax : +44 1225 385713

Abstract

Tubular alumina membranes exhibiting symmetric and asymmetric morphology were fabricated via electrochemical anodization of aluminium and studied for ultrafiltration application. By controlling the anodization conditions, the pore structure can be precisely controlled at the nanometre scale. Via reduction of the anodization voltage in a sudden or gradual manner, two types of asymmetric cross-section morphologies were obtained. The membranes were characterized by MWCO, pure water permeability, bovine serum albumin (BSA) rejection and fouling tests. The breakdown of linear relationship between anodization voltage and pore diameter was observed for anodization below 10 V. The selectivity-permeability analysis was compared to the framework developed by *Metha and Zydney (JMS, 2005)*. The analysis shows the asymmetric membranes still suffering from low permeability despite providing good rejection properties. Most of the resistance to water permeability is, however, contributed by the thickness of the support layer of the membranes. The flux decline during BSA filtration can be modelled using combined complete pore blocking –cake filtration model. Although the membranes show good rejection performance and potential for scale-up application by fabrication in tubular form, further improvement in permeability and fouling mitigation could be achieved by developing a more porous support layer and surface modification.

Keywords: Anodized alumina membrane, Ultrafiltration, Fouling, Tubular.

Research Highlights

- Fabrication of tubular asymmetric anodized alumina membranes for ultrafiltration applications
- The membranes have uniform pore structure which is readily controllable
- The membranes exhibit good bovine serum albumin rejection

1. Introduction

Ultrafiltration (UF) is widely used in many processes and industries, including waste-water treatment, the food industry and the biotechnology sector. In the latter, in particular, UF is extensively used for the concentration of bio-macromolecules, including proteins such as recombinant therapeutics and industrial enzymes [1]. Despite this success, other areas of protein purification, namely the separation and polishing steps are still dominated by packed-bed chromatography, despite its high cost, high pressure drop, low throughput and complex scale-up [2]. This is mainly due to the broad size distributions, low transport rates or poor biocompatibility of commercial nanoporous membranes [3]. An example is given by polycarbonate track etched (PCTE) membranes which have nearly mono-disperse pore size for good cut off performance, but suffer from low permeability due to low porosity (3-4%) [4]. Ceramic membranes have the potential to overcome limitations of UF polymeric membranes [4]. In particular, anodic alumina membranes (AAM), a self-ordered nanostructured material with tuneable pore size in the nanometre range, have been studied for biomolecule separation showing great potential [3].

1.1 Anodic alumina membranes

AAMs are formed by anodization of aluminium substrates in aqueous solution of acidic electrolytes, such as oxalic, sulphuric, chromic and phosphoric acids [5]. The resulting membranes have a uniform cylindrical pore structure, due to the self-ordered, closely packed hexagonal cells that can be obtained under specific anodization conditions [6]. The pore formation mechanism has been investigated in detail and is generally considered to follow a three-step process [7]: first the formation of a superficial oxide layer, followed by the formation of crack that act as pore precursors; finally, the a steady-state growth of aligned and ordered pores is obtained with a linear relation between the applied voltage and the pore diameter. This linear relation allows the fine tuning of membrane pore size with nanoscale precision in the range of 10 nm to 200nm [8]. The thickness of AAMs is also a linear function of the anodization voltage and time. The membrane porosity, on the other hand, is normally in the range of 10 to 20%, irrespective of the anodization voltage [8, 9].

These characteristics make AAMs suitable to be used as templates for the formation of nanostructured materials [10]. More recently, AAMs have been explored for separation applications including drug delivery [11], gas permeation [12] and haemodialysis [13]. Most of the previous investigations focussed on symmetric membranes fabricated by potentiostatic anodization. [14] As the thickness and pore diameter are positively related to anodization

voltage, AAMs with pores in the UF range are generally too thin to provide mechanical integrity for filtration processes [4]. This limitation can be overcome by manipulation of the voltage during anodization, resulting in asymmetric flat disk AAMs that have layers of different pore size, i.e. a thicker layer of larger pore size for support and a thin layer of small pore size for separation [12, 15]. Results have shown that continual change of anodization voltage affects the balance of the force field during the oxide growth, leading to a reorganisation of pore structure [15]. This reorganisation leads to either pore branching or blocking, by voltage reduction or increment, respectively, to keep the porosity nearly constant [16]. However, the fundamental understanding of this phenomenon is still a subject of debate and investigation. [17]

Tubular symmetric AAMs have also been prepared initially by anodizing the outer surface of an aluminium alloy tube in oxalic acid [18]. The mechanical strength of the tubular AAMs was improved by anodization of the inner surface of aluminium alloy tube [19]. The effect of anodization voltage and electrolyte type and concentration on the structural properties (pore size, interpore spacing, thickness) were found to be analogous to the flat counterpart [20]. Symmetric AAMs with average pore diameter of 15 nm were found to have superior dialysis performance compared with conventional polyethersulfone dialysis membrane, i.e. high hydraulic permeability, high solute clearance for urea, creatinine, vancomycin and inulin as well as low albumin loss (99.7% rejection) [13].

To the author's knowledge there has been no previous study on the fabrication and characterization of tubular asymmetric AAMs and their use for UF applications.

1.2 Mass transport

The transport properties of flat disk symmetric AAMs with 20 to 30 nm average pores have been studied using linear macromolecules of various molecular weight [21]. Results have shown the applicability of original pore model and that for the AAMs tested the solute sieving coefficient, S_a could be modelled as [21]:

$$S_a = \left(1-q^2\right)\left(1+2q-q^2\right)\left(\frac{1-\frac{2}{3}q^2-0.20217q^5}{1-0.75857q^5}\right) \quad (1)$$

where $q=\frac{r_h}{r_p}$, where r_h is the hydrodynamic radius of the solutes and r_p is the pore radius.

A recent study on the hydraulic permeability of pure water across AAMs by the authors has shown up to 6 times higher flow rate compared to the no-slip Haagen-Poiseuille equation in AAMs with pore size down to 20 nm [8]. This flow enhancement effect can be explained in terms of the solid-liquid molecular interactions between the liquid and the membrane material and the membrane characteristic dimensions, namely thickness and pore diameter [22].

To compare the performance of various UF membranes commercially available, a graphical framework has been developed based on permeability-selectivity analysis using bovine serum albumin (BSA) as a model sieving solute [23]. The permeability-selectivity trade-off curve clearly shows that polymeric membranes outperform commercial ceramic ones. This is mainly attributed to the significantly lower porosity to thickness ratio, ε/L of ceramic membranes [23]. Despite having inferior performance, inorganic membranes still hold the advantage in terms of biocompatibility, chemical and biological inertness [4, 23]. The study was further improved by considering a 'scaled permeability, β' to account for membranes with different pore geometry [24]. Using scaled rather than absolute permeability allows exploring the potential of the membranes, giving insight on how further engineering of the membrane structure (porosity and length) could improve the actual permeability of the membrane.

1.3 Membrane fouling

Membrane-protein interaction inevitably leads to fouling which greatly reduces the throughput or increases the energy consumption to generate higher transmembrane pressure. Understanding the fouling mechanism can provide information on how to modify the membranes accordingly to minimise the fouling effect or develop an appropriate cleaning strategy. Declining flux in dead-end filtration can generally be described by four classical fouling models, namely complete, intermediate and standard pore blocking, and cake filtration [25]. In the cake filtration model, fouling results in deposition on the external surface of the membrane that increases its thickness over time. This provides an additional resistance to flow in series with that of the membrane. In the other three models, the membrane is assumed to be composed of a parallel array of cylindrical pores with uniform pore size. When the solute size is significantly smaller than membrane pore size, the standard pore blocking model is used to describe the fouling occurring within the membrane leading to a reduction in the effective pore size. The complete and intermediate pore blocking models assume that the pores are occluded by the foulant, with the latter model accounting for

particle superimposition on the external membrane surface [26]. Although these classical models are most often used for analysis, there is considerable experimental evidence showing a transition in the fouling behaviour, with the initial flux decline associated with pore blocking followed by cake formation [27]. Previously, BSA fouling behaviour on pristine and surface modified 200 nm flat disk symmetric AAMs (commercial Anopore^{TM} membranes) showed good agreement with the standard pore blocking model [28]. This can be attributed to the fact that the membrane pore diameter is at least 20 times bigger than the size of BSA.

In the current work, both symmetric and asymmetric tubular AAMs were fabricated with a range of anodization parameters, resulting in membranes in the UF range with narrow pores sizes from about 50 to below 10 nm. The morphology of the membranes and pore size distribution was characterized by electron microscopy and MWCO measurements. Hydraulic permeability and BSA filtration were performed to compare the permeability and selectivity performance with other UF membranes. Finally, fouling tests were performed on AAMs with average pore diameter comparable to the BSA size to investigate their suitability for UF applications.

2. Materials and method

2.1 Membrane fabrication

Tubular AAMs were prepared using an anodization procedure derived from the well-established one for flat sheet membranes: A1050 grade aluminium alloy tubes (>99.5% Al, Haynes Tube), having length, outer diameter and thickness of 90 mm, 6.35 mm and 0.3 mm, respectively, were first annealed in air at 500 °C for an hour. Then, the tubes were cleaned by ultra-sonication in acetone (99.5+%, Sigma) for 10 min. The inner surface of the cleaned tubes was electro-polished with a solution of perchloric acid (60-62%, Sigma) and ethanol (96%, Sigma) in the volumetric ratio of 1:4. Using a dry ice-acetone bath to maintain the temperature (<-50°C), the electro-polishing was performed at 20 V for 30 min to obtain a mirror-like shiny surface.

A one-step anodization was used in this paper [14]. As shown schematically in Figure 1, the inner surface of the aluminium alloy tube is anodized by recirculating the electrolyte using a peristaltic pump. Depending on the desired pore diameter of the AAMs, the anodization parameters such as electrolyte type and concentration, voltage, temperature and time were chosen based on the specific conditions within the well-established self-assembly regime [5]. In this work, 0.5 M sulphuric acid (diluted from 5M solution, Aldrich) was used for anodization voltages of 20 - 25 V, whereas 1.0 M concentration was used for any anodization below 20 V. Oxalic acid (0.3 M, prepared from anhydrous form, >99%, Sigma-Aldrich) was used in some cases to prepare AAMs for morphological studies. The anodization temperature was carefully monitored and the pump rate was optimized to prevent ion depletion and overheating within the tube due to the exothermic nature of the reaction. The apparatus had been optimised to allow hydrogen gas, a by-product of anodization, to vent off easily from the top plug.

Both symmetric and asymmetric AAMs were prepared. Potentiostatic anodization was performed to fabricate symmetric membranes, in the range of 10 V to 25 V (using a DC power supply 6645A from Agilent). As the membrane thickness is linearly related to current density and hence the voltage, the anodization for symmetric membranes was performed for 10 to 24 hours, depending on the voltage, to obtain mechanically robust membranes [8]. However, anodization below 10 V does not yield sufficiently thick membranes that are mechanically rigid to be handled. Therefore, asymmetric membranes were prepared with 12 hours of initial anodization at 18 V and then gradually ramped down to a final voltage (1, 2 or 5 V) which was maintained for minimum 4 hours. The reduction rate of the anodization

voltage was 0.005V s^{-1} to provide sufficient time for anodic cell geometric re-organisation [29]. Conditions of membrane preparations are summarised in Table 1. Multiple samples were prepared for each condition for different characterisation and testing.

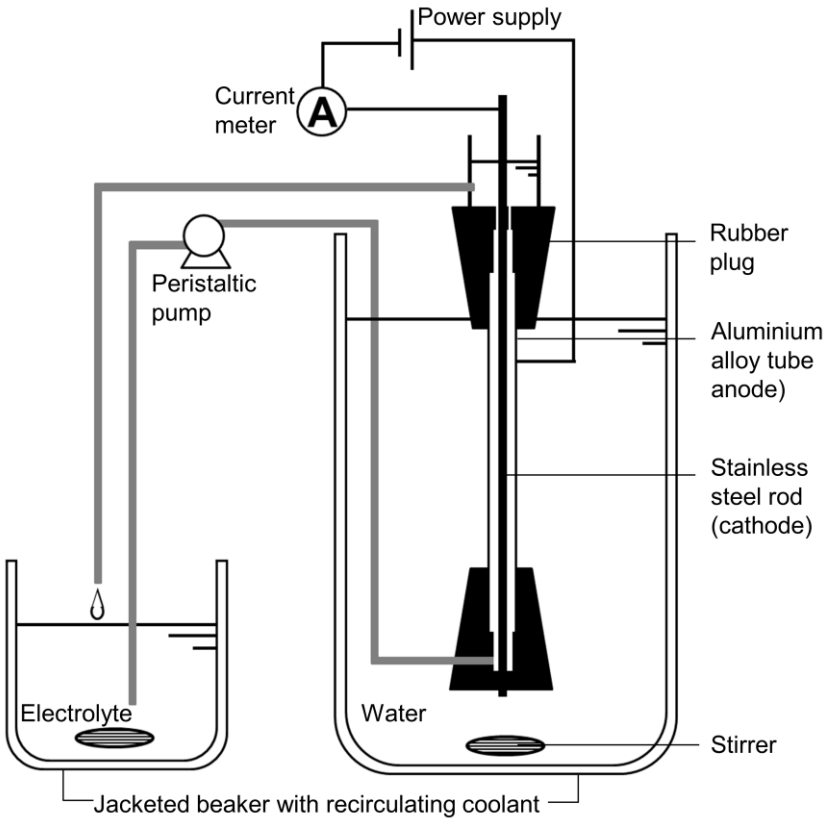

Figure 1. Anodization apparatus for tubular AAMs.

Table 1. Conditions of AAMs anodization

Sample	Voltage (V)		Electrolyte	Temperature	Ramp rate	Time (hr)		Thickness
	Initial	Final		(°C, ±1)	(V s^{-1})	Initial	Final	(μm, ±1)
Symmetric AAMs								
S25	25	-	0.5 M H_2SO_4	0	-	10	-	71
S20	20	-	0.5 M H_2SO_4	0	-	12	-	32
S15	15	-	1.0 M H_2SO_4	0	-	18	-	38
S12	12	-	1.0 M H_2SO_4	0	-	20	-	27
S10	10	-	1.0 M H_2SO_4	0	-	24	-	21
Asymmetric AAMs								
A18-5	18	5	1.0 M H_2SO_4	0	0.005	12	4	56
A18-2	18	2	1.0 M H_2SO_4	0	0.005	12	4	53
A18-1	18	1	1.0 M H_2SO_4	0	0.005	12	4	50
A40-5	40	5	0.3 M $H_2C_2O_4$	13	0.01	10	4	55
A40-20[a]	40	20	0.3 M $H_2C_2O_4$	13	0.2[a]	10	2[a]	55

[a] A40-20 was ramped down quickly to 20 V with an intermediate stage of 28 V. The voltage was maintained for 2 hour before being ramped down to final 20 V.

After anodization, a 50 mm long section of the residual non-anodized aluminium on the outside of the tube was removed by a reaction with copper(II) chloride in a 1:1 solution of 0.2 M copper(II) chloride (prepared from >99% copper (II) chloride dehydrate, ACS reagent) and 20 wt% hydrochloric acid (37%, ACS regent). The 20 mm-long outer ends of the aluminium tube were protected using adhesive tape to provide for membrane handling. Finally, the oxide barrier layer, formed at the bottom of the pores (i.e. the external surface), was etched away by 6 wt% phosphoric acid (85%, Sigma-Aldrich) at 25°C. Experiments had been performed to optimise the etching time, ensuring that the porous structure is completely opened with no over-etching (See supplementary information) [8].

2.2 Membrane characterisation and testing

2.2.1 Membrane morphology

AAM pore characterization by various direct measurement techniques such as liquid-liquid displacement, nitrogen or mercury adsorption is not practical due to the sample mass being too small to give statistical meaningful results. As such, AAMs are usually characterized via statistical image analysis of high resolution scanning electron microscope (SEM) micrographs [30]. In this work a JEOL 6301F field emission SEM was used with low accelerating voltage and short working distance settings to minimise charging on the membranes, negating the need for a conducting coating. This approach enabled the direct observation of the topography and cross-section of the membranes. Standard image analysis processing using ImageJ® was applied to determine the mean pore diameter and porosity [8]. Membrane thickness was observed by analysis of FE-SEM micrographs of the membrane cross-sections by taking average of three readings per membrane.

2.2.2 Pure water permeability

Pure water permeability of the AAMs was measured using a custom made mini ‘shell and tube’ module (See supplementary information). One end of the tubular AAMs was sealed with silicone sealant to facilitate dead-end permeation. According to Darcy’s law, the flux through the membrane (J), can be related to the transmembrane pressure (ΔP), the viscosity of water (μ), the thickness and porosity of the membrane (L, ε) via the scaled hydraulic permeability (β) [24]:

$$\beta = \frac{\mu L J}{\varepsilon \Delta P} \tag{2}$$

2.2.3 Molecular weight cut off (MWCO) determination

To further validate pore size distributions obtained via image analysis of FE-SEM micrographs, MWCO tests were carried out to characterise the separation ability of the asymmetric AAMs. The pore size of the asymmetric membrane can be correlated based on the following equations [31, 32]:

$$d_{50} = 0.11\left(MW_{50}\right)^{0.46}$$
$$d_{90} = 0.066\left(MW_{90}\right)^{0.46} \quad (3)$$

where d_{50} is the mean pore diameter (in nm), d_{90} is the diameter (in nm) of the solute that is 90% rejected, (i.e. large proportion of pores have diameter less than d_{90}), MW_{50} and MW_{90} are the molecular weight of the solute that displays 50% and 90% rejection capability, respectively. The similarity in d_{50} and d_{90} indicates a narrow pore size distribution.

For MWCO tests, 10 kDa polyethylene glycol (PEG, Aldrich), and 27.8, 51.5, 95 and 140 kDa polyethylene oxide (PEO, Phenomenex) were chosen as the solutes. To avoid interaction among the solutes of different molecular weight, filtration was carried with a new sample each time with the solution containing a single solute at the concentration of 1000 mg L^{-1}. Ultrapure DI water (Millipore) with 0.05 wt% sodium azide (99%, Sigma) added was used to prepare the solutions. Using filtered compressed air, dead end filtrations were performed using 50 kPa for the feed entering at the shell-side and permeate through the membrane in the inner bore. Each experiment was run for an hour and permeates were collected at 10 minute intervals. The feed and permeate samples were analysed using a High Performance Liquid Chromatography (HPLC) system (Shimadzu, SCL-10A_{VP} system controller, SIL-10AD_{VP} auto injector, LC-10AD_{VP} liquid chromatograph, RID-10A refractive index detector) with an incorporated size exclusion column (TSKgel G3000PW). A calibration curve was obtained by measuring the elution time for each feed solution. The flow rate through the column was set to 0.8 ml min^{-1}.

2.2.4 BSA filtration

The BSA (>98%, Sigma-Aldrich) solution was prepared at the concentration of 1000 mg L^{-1} in phosphate buffer saline (PBS, Sigma, pH 7.4) with 0.05 wt% sodium azide. The unused solution was stored refrigerated at 4°C for less than a week. The parameters for BSA filtration tests were similar to MWCO test, including transmembrane pressure. Exceptionally only 20 kPa was applied for S10 and S12 membranes because these

membranes are insufficiently strong to withstand higher pressure. The BSA concentration was analysed by a well-established spectrophotometric method where UV light absorbance of the samples at 280 nm was measured (Shimadzu UV-1601)[33]. The average of three repeated readings was taken for each sample.

The observed sieving coefficient (S_o), actual sieving coefficient (S_a) and rejection (R) can be obtained by:

$$S_o = \frac{C_P}{C_F};\ S_a = \frac{S_o}{(1-S_o)e^{\frac{J}{k}} + S_o};\ R = 1 - S_o \tag{4}$$

where C_P and C_F are the concentration of BSA in permeate and feed, respectively; J is the flux and k is the mass transfer coefficient for different modules [34].

2.2.5 Modelling of BSA fouling

The BSA fouling test was only performed on asymmetric membranes as they offered superior BSA rejection compared to results for symmetric ones . The experiments performed were similar to that of BSA filtration, with a couple of differences. First, the inner bore of the membrane (permeate side) was prefilled with clean PBS. This was done to eliminate the lag time for the permeate to fill the tube bore, as the initial change in flux is crucial for fouling modelling. Second, the permeate was collected in a beaker placed on a high precision balance (Mettler Toledo, MS304S/01, 0.1mg precision). The beaker was pre-filled with oil to minimise water loss by evaporation. All real-time measurements, *i.e.* pressure, temperature and mass of water permeate were recorded *via* a data acquisition system. The experiments were performed for 4 to 20 hours at 100±2 kPa and 21±1°C. SigmaPlot 12.3 was used for fitting of data into the fouling model.

3. Results and discussion

3.1 Membrane morphology

Figure 2a shows an optical image of a 10 V symmetric tubular AAM; it can be observed that the membrane, 21 μm thick, is translucent. As discussed in the introduction, the linear dependence of the average pore diameter on the anodization voltage is similar to that of flat symmetric AAMs [7], with porosity in the 10-15 % range. The one step anodization process used here results in a slightly less uniform top surface, which corresponds to the permeate side in this work (Figure 2b to 2d) [8]. No noticeable change in pore size distribution was observed when using a significantly less expensive aluminium alloy instead of high purity

aluminium. This is a significant result in view of a potential commercial use of these membranes. From image analysis, the mean pore diameter for AAMs anodized at 40 V, 20 V and 10 V is 47 ± 2 nm, 25 ± 1 nm and 10 ± 3 nm, respectively. The optimum anodization voltage for self-assembly pore structures fabricated by oxalic acid and sulphuric acid is 40 V and 20 V, respectively [6]. Therefore, the pores in the 40 V and 20 V membranes have higher circularity than others. Nevertheless, narrow pore size distributions were obtained for all AAMs tested. The use of one-step anodization does not affect the membrane selectivity despite the less uniform structure of the support layer because the uniform pore structure of the active layer, which is responsible for selectivity, is the same for one- and two-step anodizations [6, 7].

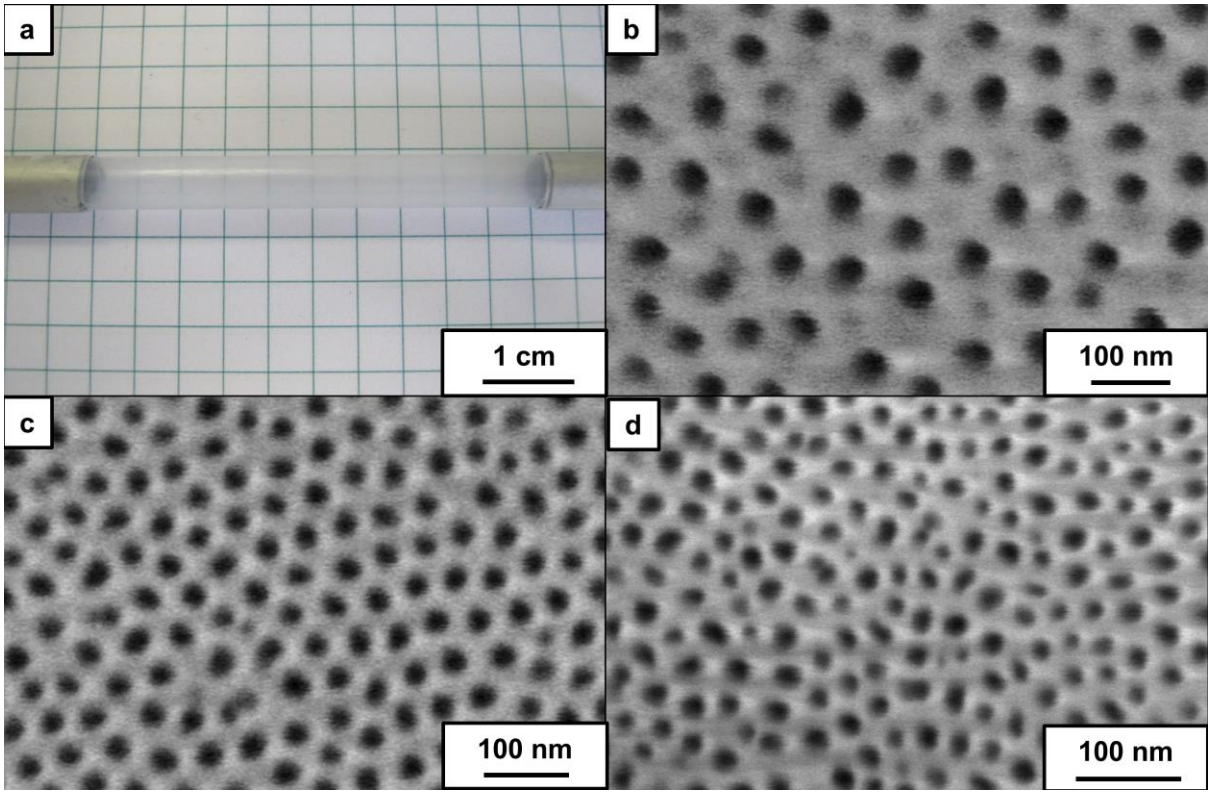

Figure 2. a) A symmetric tubular AAM after anodization (at 10 V), with a 50 mm long section where residual non-anodized aluminium and oxide barrier layer have been removed. The SEM micrographs showing the top surface (the surface where the anodization started, permeate side in the present paper) of (b) A40-5; (c) S20 and (d) S10.

Asymmetric AAMs were fabricated by controlling the voltage during the anodization. Two strategies were used to reduce the diameter: First, the anodization voltage was suddenly reduced by a factor of $2^{-0.5}$ to create Y-branched pores, i.e. one pore channel is branched into

two [15]. An example of the morphology obtained with this method is shown in the SEM micrograph of the cross-section of sample A40-20 (Figure 3a). Figure 3b, shows the symmetric region of the membranes with straight pores (40 V potentiostatic anodization). Figure 3c illustrates the transition where the sudden change in anodization voltage leads to the branching and re-organisation of porous structure, with the y-branching shown in Figure 3d. The thickness of this section can be controlled via the anodization time. Further reduction of the anodization voltage by the same factor will lead to another generation of pore branching. *n* branches can be achieved by reducing the anodization voltage by a factor of $n^{-0.5}$ where n = 2, 3, 4, 6, 8, 16 [15].

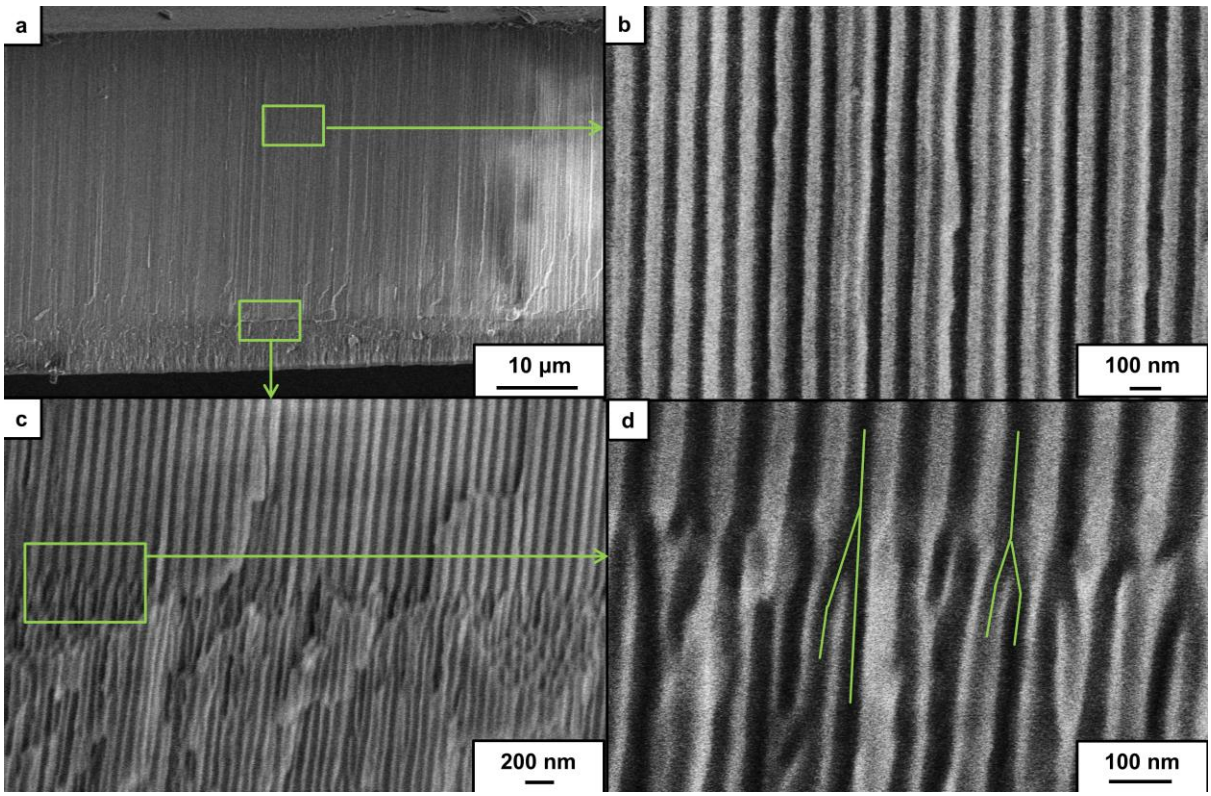

Figure 3 SEM micrographs showing the cross-sections of A40-20 AAM at different level of magnification, where (a) shows the overall thickness of the AAM; (b) the cross-sectional zone where a symmetric structure was obtained at the initial potentiostatic condition; (c) the cross-sectional zone where the sudden reduction of anodization voltage from 40 V to 28 V led to smaller pores and (d) is a close-up image showing pore y-branching.

The second strategy involved a slow constant anodization voltage ramp down rate to the final anodization voltage. As shown in Figure 4a, the development of branching pores happens gradually at several depths from the membrane surface. It can be clearly seen that

the average pore size decreases from left to right in Figure 4a, leading to smaller pores with higher density when moving to the right. On the right side the membrane section where the final anodization voltage was maintained for a period of time to form the active layer of the AAMs can be observed. The voltage ramp down rate has to be slow as previous studies have shown that fast ramp rates (> 0.1 V s^{-1}) lead to disordered structures due to an insufficient time for pore structure reorganisation, especially towards the lower end of anodization voltage [29]. Figure 4b shows the membrane active layer thickness, which is determined by the hold time at the final anodization voltage.

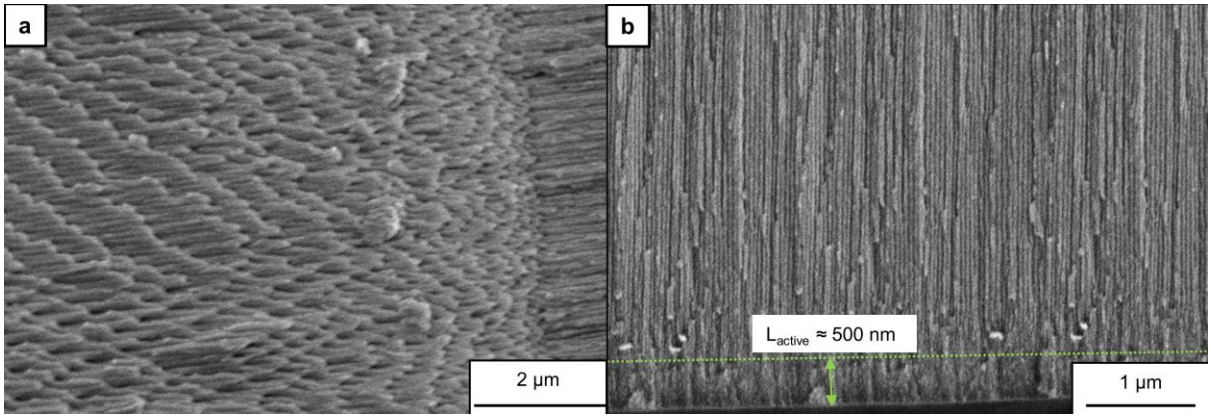

Figure 4 SEM micrographs showing the cross-sections of (a) A40-5 and (b) A18-2. (a) shows the continual pore branching along the radial direction, from the inner to the outer surface, over the course of gradual anodization voltage reduction and (b) shows the thickness of selective layer formed by final anodization voltage.

As tabulated in Table 1, the thickness of symmetric membranes varies significantly according to the anodization voltage and electrolyte concentration [35]. As discussed, this means also that the thickness of membranes fabricated at low voltage, i.e. S10 and S12, is very low. While conducting water permeability measurements, these membranes failed before reaching 50 kPa of hydraulic pressure. In contrast, the asymmetric AAMs fabricated have a thickness higher than 50 µm, mainly contributed by the support layer formed during the initial anodization at higher voltage. While offering similar or even superior separation performance compared to low voltage symmetric one (see Section 3.2), asymmetric membranes are mechanically stronger for practical applications, with stability up to 200 kPa of hydraulic pressure during water permeability measurement.

3.2 Selectivity–permeability analysis

3.2.1 MWCO of asymmetric AAMs

Two asymmetric AAM samples were prepared for each specific anodization condition (Table 1). The MW_{50} and MWCO are both tabulated in Table 2 (See supplementary information for MWCO curves). All six membranes tested provide very similar MWCO values. The cut-off curves of four membranes are very sharp, indicating a narrow pore size distribution as would be expected. Though having a less sharp cut-off curve, the other two samples are still considered to have a narrow pore size distribution when comparing to commercial ceramic UF membranes with similar pore size range [36]. While this wider pore size distribution has led to a doubling of the MWCO value compared to the other four samples, very similar rejection properties are observed for all asymmetric AAMs tested, irrespective of the different final anodization voltage. An average pore diameter for the skin layer of 10 ± 2 nm was calculated from MWCO data using the two models in equation 3. This result confirms previous observations of a breakdown of the linearity between anodization voltage and pore diameter below the anodization voltage of 10 V [37], with a minimum attainable pore size of about 10 nm. This result also explains why different MWCO for the asymmetric membranes do not give rise to different separation performance.

The concentration of permeates collected at different time intervals was compared and showed reproducible and compatible readings within the sensitivity margin. This shows that any effect of solute deformation or concentration polarization during the test time is negligible.

Table 2 MWCO values of asymmetric AAMs and the pore diameter estimation based on equation 3.

Sample[a]	MW_{50} (±1000)	MWCO (±1000)	d_{50} (±1nm)	d_{90} (±1nm)
A18-1a	21000	40000	11	9
A18-1b	24000	7400	11	11
A18-2a	2200	43000	11	9
A18-2b	21000	43000	11	9
A18-5a	23000	44000	11	9
A18-5b	27000	75000	12	12

[a]Two samples per anodization conditions were prepared and labelled ‘a’ and ‘b’, respectively.

3.2.2 Selectivity-permeability trade-off curve

The results of the permeability-selectivity measurements are reported in Table 3. The rejection of BSA by S25 and S20 remains low due to their relatively large pore size compared to the hydrodynamic diameter of BSA, which is about 7.3 nm [24]. The higher rejection (21%) of one of the S25 samples is likely due to the incomplete removal of the barrier layer, causing the outer surface to have a smaller pore diameter as evidenced by the lower hydraulic permeability. As the pore diameter is reducing, the rejection of BSA is increasing as expected. It is especially obvious when the pore diameter of the membrane is below 20 nm. Nevertheless, the rejection of BSA by symmetric AAMs did not go beyond 90% for effective separation. For asymmetric AAMs, all membranes bar one have achieved consistently higher than 90% BSA rejection. The odd result could be attributed to the structural defects present in the specific membrane, in analogy to the one in the MWCO test (See supplementary information).

When converting the observed sieving coefficients into actual ones using equation 4, there was no noticeable difference. This is mainly due to the membrane flux being small and hence the denominator of the equation approaching unity. As for the hydraulic permeability, there is no observable correlation with pore diameter or anodization condition. While the pore model generally estimates that the hydraulic permeability is inversely correlated to the square of the pore diameter, this was not observed in this study due to the complexity of the membrane thickness and possible flow enhancement effects [8], which both affect permeability. The lower the anodization voltage is, the lower the membrane thickness is. In addition, earlier experimental studies by the authors concluded that the flow enhancement effect increases with decreasing pore diameter, especially when the average pore diameter is below 30 nm [8]. Therefore, the overall permeability of AAMs does not show a significant trend with anodization condition.

One interesting point to be noted is that the asymmetric AAMs have higher than expected permeability. Unlike polymeric asymmetric membranes where the skin layer accounts for most of the transport resistance, the major contribution in the asymmetric AAMs is still given by the support layer with has double the pore size of the active layer and accounts for 97.5% of the total membrane thickness (about 20 μm), This translates, using the Haagen-Posieuille equation separately for the support and active layer, in the former accounting for more than 90% of the total membrane resistance (see supplementary

information for details and calculations). This value could be even higher if the presence of flow enhancement in the active layer was considered [8].

Table 3 The measured pure water permeability and BSA rejection. Multiple samples have been tested for each anodization condition.

Samples	BSA rejection[a]	Observed and actual sieving coefficient	Separation factor	Hydraulic permeability ($\times 10^{-9}$ m s^{-1} Pa^{-1})
S25	0.03	0.97	1.03	0.17
	0.09	0.91	1.10	0.14
	0.01	0.99	1.01	0.17
	0.21	0.79	1.27	0.05
S20	0.17	0.83	1.20	0.24
	0.25	0.75	1.34	0.20
	0.21	0.79	1.27	0.20
S15	0.61	0.39	2.54	0.17
	0.54	0.46	2.15	0.17
	0.56	0.44	2.27	0.10
S12	0.72	0.28	3.52	0.15
	0.59	0.41	2.47	0.19
S10	0.86	0.14	7.25	0.11
	0.83	0.17	5.84	0.10
A18-5	0.93	0.07	13.53	0.12
	0.93	0.07	14.22	0.12
	0.94	0.06	16.84	0.08
A18-2	0.96	0.04	26.60	0.13
	0.98	0.02	58.14	0.15
	0.92	0.08	12.44	0.22
A18-1	0.98	0.02	48.31	0.14
	0.80	0.20	4.94	0.19
	0.99	0.01	84.75	0.12

[a] Given a sensitivity of up to 20 mg L^{-1} for the photometric method used for the BSA concentration determination, the error for the BSA rejection is ± 0.02 for a BSA feed solution concentration of 1000 mg L^{-1}.

The data tabulated in Table 3 has been included into the UF membranes comparison framework developed by Mehta and Zydney [23], as shown in Figure 5. Due to the significant membrane thickness, the AAMs are less permeable than polymeric membranes. However, the selectivity compares well to that of polymeric membranes, and the separation performance of AAMs is superior to that of any other ceramic membrane included in the plot.

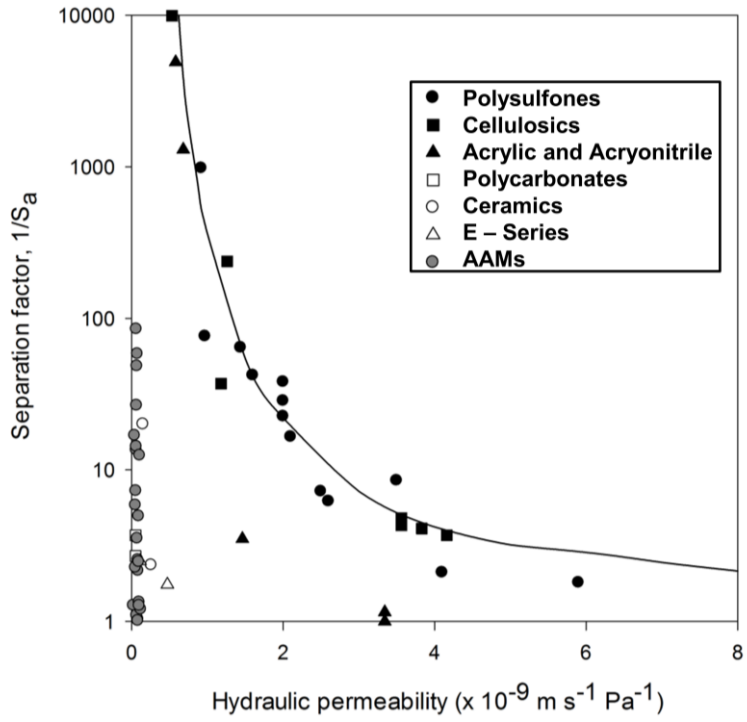

Figure 5 Selectivity-permeability trade-off for ultrafiltration membranes using BSA as the model protein. (Adapted from [23])

While the previous plot provides a straight forward framework for UF membrane comparison, Kanani et al. later replaced hydraulic permeability with a scaled permeability to observe the effect of pore geometry on membrane performance [24]. Data for both symmetric and asymmetric AAMs was re-arranged to fit this new framework assuming a porosity equal to 0.20 (the most conservative value within the experimental range of 0.10-0.20) and considering the total thickness of the AAMs (Figure 6). For the asymmetric AAMs, the total thickness is still used in lieu of the skin layer thickness alone due to the fact that the support layer of the membrane is still the major contributor to transport resistance, as discussed above. Experimental data in Figure 6 is compared to a theoretical model (solid curve) derived by calculating the scaled permeability via the Hagen-Poiseuille equation and the separation via equation 1 for a range of corresponding pore diameter and taking the hydrodynamic diameter of BSA to be 7.3 nm [24]. While Figure 5 provides a framework to compare UF membranes' practical performance, Figure 6 enables the comparison between the theoretical and experimental performance of the membranes. It can be observed that the performance of symmetric AAMs is generally following the theoretical trend, with most of the data points falling on the right side of the theoretical curve. This can be explained by the flow enhancement effect, where previous studies have shown more than doubling of the flow

enhancement in AAMs with pore diameter 30 nm and below [8]. For asymmetric AAMs, the performance appears to be superior to the prediction of the theoretical model. This is attributed to the asymmetric structure of the membrane: The presence of an active layer with smaller pore diameter has substantially improved the separation performance of the membrane without compromising the permeability of the membrane, as discussed before. This has therefore shifted the membrane separation factor upwards, beyond the theoretical model curve.

These results suggest that the performance of asymmetric AAMs can be enhanced by improving the permeability of the support layer. While this could be achieved by increasing the pore diameter and porosity of the support layer, via the anodization voltage, the ramp rate used to achieve the final anodization voltage has to be optimized [15]: If the ramp rate is too high, branching will occur due to the inability of the pore structure to adapt fast enough. If the ramp rate is too slow, the increased thickness of the transition section will negate any meaningful increase in permeability.

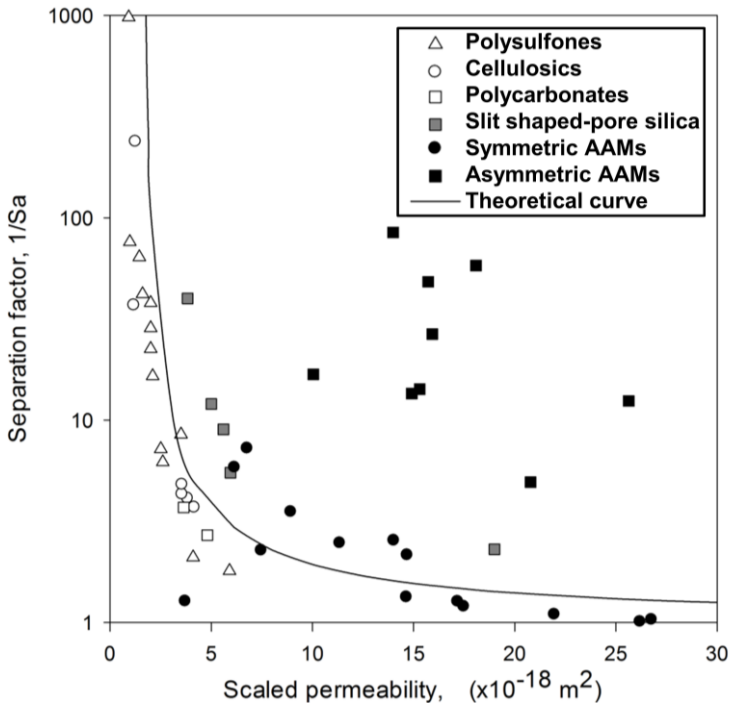

Figure 6 Selectivity-permeability trade-off for ultrafiltration membranes using BSA as the model protein. The line curve is plotted based on theoretical pore model. (Adapted from [24])

3.3 Fouling modelling

Since only the asymmetric AAMs show promising results for separation of BSA, fouling tests were not performed on symmetric AAMs. Model fitting was performed on the

cumulative permeate volume profiles to understand which fouling mechanism dominates the flux decline. Of the four classical fouling mechanisms found in the literature [21], none of them provided a satisfactory fitting for the data. Therefore, combined fouling models were investigated instead. The results indicate that the complete pore blocking – cake filtration model consistently gives the most satisfactory fittings over the range of data obtained (Figure 7), with R^2 consistently higher than 0.99. The complete pore blocking – cake filtration model can be described by the following equation with steady-state flux being taken into account [27, 34]:

$$V = \frac{J_0}{K_b}\left(1 - e^{\frac{-K_b}{K_c J_0^2}\left(\sqrt{1+2K_c J_0^2 t}-1\right)}\right) + J_{ss}t \tag{5}$$

where V is the accumulated permeate volume (m^3 m^{-2}), J_0 is the initial flux (m s^{-1}), J_{ss} is the flux at steady-state (m s^{-1}), K_b is the complete pore blocking constant (s^{-1}), K_c is the cake filtration constant (s m^{-2}), and t is the time (s).

There is ample evidence in the literature that the type of combined fouling behaviour discussed here can occur either in sequence or simultaneously [26]. In the former case, the initial flux decline is dominated by the pore blocking mechanism followed by cake filtration, with the formation of cake layer facilitated by the pore blockage. In the latter case, the flux decreases through a reduction in area by complete pore blockage or an increase in resistance through caking or cake thickening [27]. When K_b is high, flux decline is dominated by complete pore blocking whereas the cake filtration mechanism is dominating when K_c is high. It is obvious to see that in Figure 7a, when K_b is high, the flux declines sharply as shown by the corresponding curve in Figure 8. This can be attributed to the initial rapid loss of available pore area. In Figure 7b and d, K_c is large, with cake formation dominating and resulting in relatively low steady-state flux as compared to the other two cases. For the case in Figure 7c, both mechanisms contribute to the flux decline. The different flux decline behaviour among different asymmetric AAMs (including membranes fabricated under the same anodization conditions) is likely due to structural differences between the membranes: For example, slightly over-etching of the skin layer would cause pore widening for a certain depth in the active layer. When filtration is performed, the solute will be able to enter the pore until it is blocked by the non-widened part of the active layer. This will reduce the likelihood of cake formation. Other reasons can include the presence of defects within the membrane or incomplete removal of the oxide barrier layer.

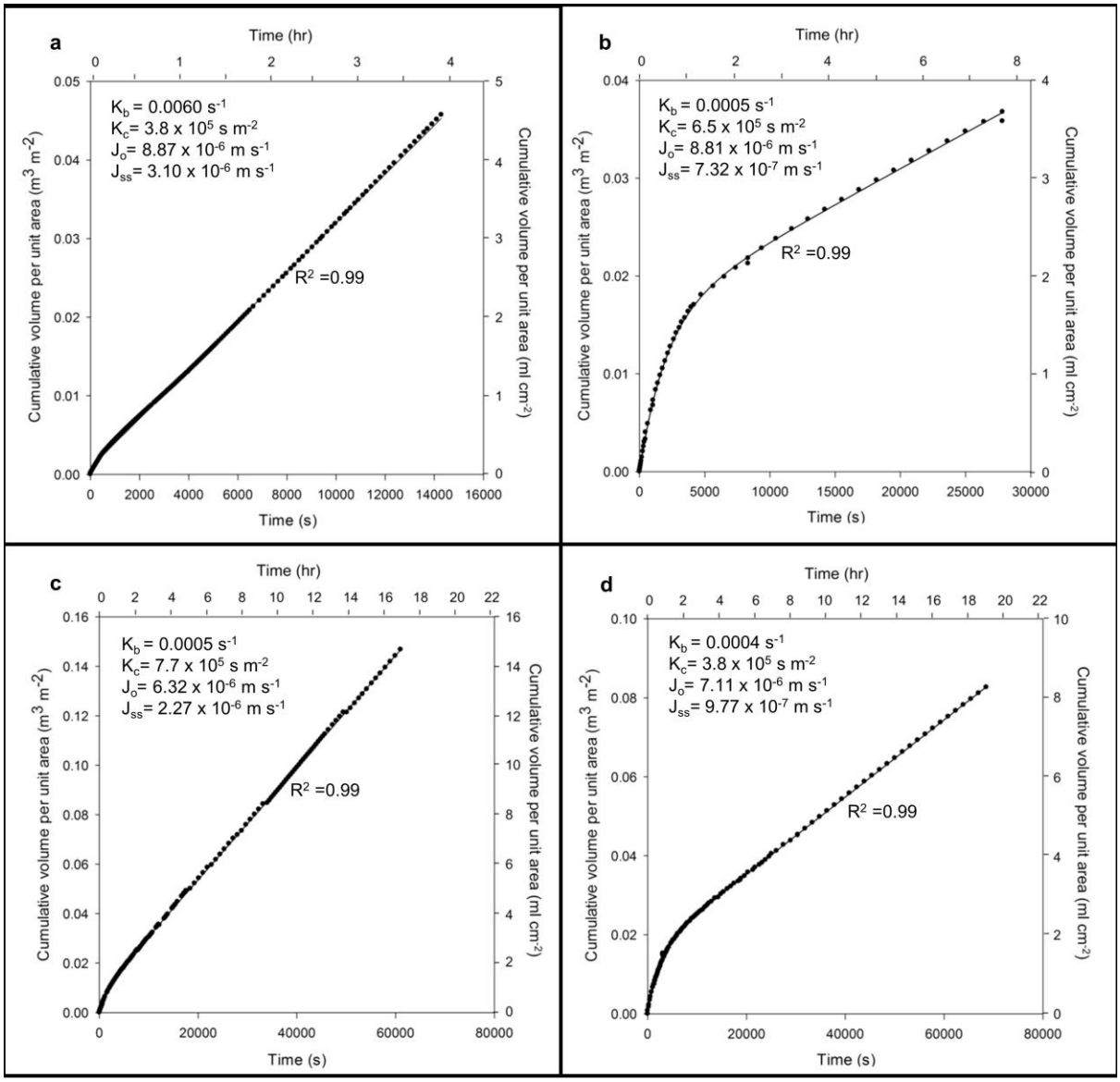

Figure 7. The cumulative permeate profiles during BSA filtration and the data fitted by the complete pore blocking – cake filtration model with fitting parameters are labelled for different asymmetric membranes: (a)A18-2a; (b)A18-1; (c)A18-5 and (d) A18-2b. See Table 1 and 2 for details on the structure of these membranes.

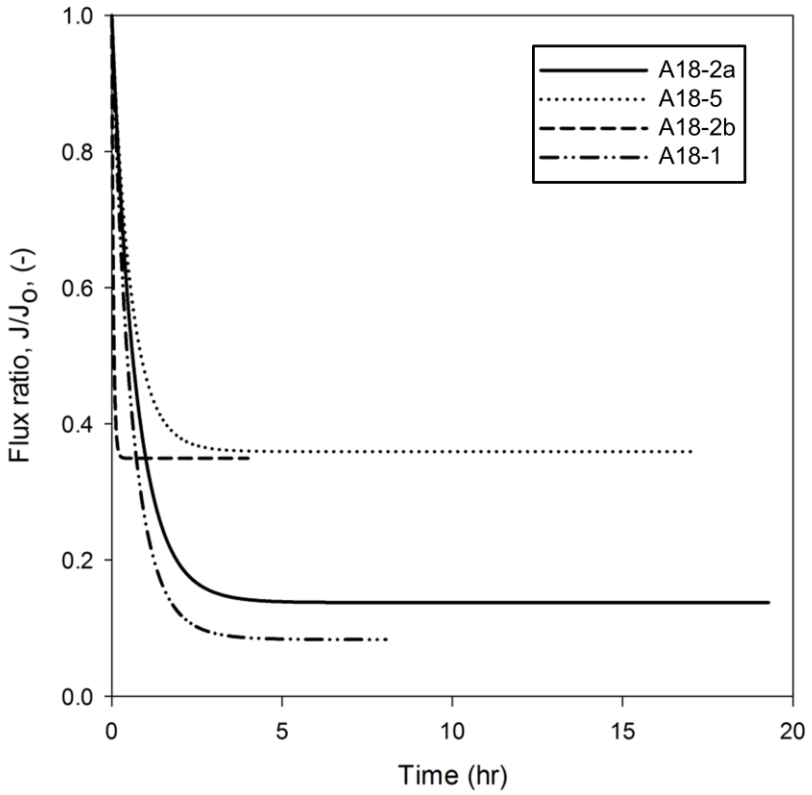

Figure 8 Flux decline profile over the course of BSA filtration.

4. Conclusions

In this study, both symmetric and asymmetric tubular AAMs have been successfully fabricated. Despite the use of an aluminium alloy, the resulting porous structure obtained is similar to membranes obtained using highly pure - and more expensive - aluminium. The MWCO tests show consistent separation results for asymmetric AAMs with average pore size of 10 ± 2 nm, showing a breakdown of the linear dependence of the pore diameter with anodization voltage below 10 V. While most symmetric AAMs show limited rejection of BSA, asymmetric AAMs reliably reject more than 90% of BSA. As for selectivity-permeability analysis, the asymmetric AAMs outperform other commercial ceramic membranes although they still have very low flux relative to polymeric ones. On the other hand, selectivity-scaled permeability analysis shows great potential for asymmetric AAMs if the porous structure of the support layer can be engineered to improve the permeability. The flux decline during BSA filtration can be described by combined complete pore blocking-cake filtration model. Further improvements such as surface modification by coating or grafting are needed to mitigate fouling and bring AAMs to commercial application.

Nomenclature

C_F, C_P	concentration of BSA in the feed and permeate, respectively, (mg L^{-1})
d_{50}, d_{90}	mean pore diameter or diameter of the solute that is 50 and 90% rejected, respectively (nm)
J, J_o, J_{ss}	flux, initial flux and steady-state flux, respectively (m s^{-1})
k	mass transfer coefficient (m s^{-1})
K_b, K_c	constants for complete pore blocking (s^{-1}) and cake filtration (s m^{-2}), respectively
L	membrane thickness (m)
MW_{50}, MW_{90}	molecular weight of the solute that shows 50% or 90% rejection, respectively (Da)
ΔP	transmembrane pressure (Pa)
q	the ratio of r_h to r_p (-)
R	fraction of solute rejection (-)
r_h	hydrodynamic radius of solute (nm)
r_p	pore radius (nm)
S_a	actual sieving coefficient (-)
S_0	observed sieving coefficient (-)
t	time (s)
V	accumulated permeate volume per unit membrane area (m)
β	scaled hydraulic permeability (m^2)
ε	porosity (-)
μ	viscosity (Pa s)

Acknowledgement

The authors would like to acknowledge the University of Bath for supporting this work via the award of an Overseas Research Student Excellence Scholarship to Kah Peng Lee. Additionally we acknowledge the UK EPSRC (grant EP/G045798/1) and the EU (grant PIRG03-GA-2008-230876) for funding support. The contents reflect only the authors' views and not the views of the European Commission.

References

[1] R. van Reis, A. Zydney, Membrane separations in biotechnology, Curr. Opin.Biotechnol., 12 (2001) 208-211.
[2] E.N. Lightfoot, J.S. Moscariello, Bioseparations, Biotechnol. and Bioeng., 87 (2004) 259-273.
[3] H.U. Osmanbeyoglu, T.B. Hur, H.K. Kim, Thin alumina nanoporous membranes for similar size biomolecule separation, J Mem. Sci., 343 (2009) 1-6.
[4] P. Stroeve, N. Ileri, Biotechnical and other applications of nanoporous membranes, Trends biotechnol., 29 (2011) 259-266.
[5] O. Jessensky, F. Muller, U. Gosele, Self-organized formation of hexagonal pore arrays in anodic alumina, Appl. Phys. Lett., 72 (1998) 1173-1175.
[6] W. Lee, R. Ji, U. Gosele, K. Nielsch, Fast fabrication of long-range ordered porous alumina membranes by hard anodization, Nat Mater, 5 (2006) 741-747.
[7] J.P. O'Sullivan, G.C. Wood, The morphology and mechanism of formation of porous anodic films on aluminium, P Roy. Soc. Lond.. A. Mat., 317 (1970) 511-543.
[8] K.P. Lee, H. Leese, D. Mattia, Water flow enhancement in hydrophilic nanochannels, Nanoscale, 4 (2012) 2621-2627.
[9] K. Nielsch, J. Choi, K. Schwirn, R.B. Wehrspohn, U. Gösele, Self-ordering regimes of porous alumina: The 10% porosity rule, Nano Lett., 2 (2002) 677-680.
[10] C.R. Martin, Nanomaterials: A membrane-based synthetic approach, Science, 266 (1994) 1961-1966.
[11] D. Gong, V. Yadavalli, M. Paulose, M. Pishko, C.A. Grimes, Controlled molecular release using nanoporous alumina capsules, Biomed. Microdevices, 5 (2003) 75-80.
[12] H.d.L. Lira, R. Paterson, New and modified anodic alumina membranes: Part III. Preparation and characterisation by gas diffusion of 5 nm pore size anodic alumina membranes, J Mem. Sci., 206 (2002) 375-387.
[13] A.C. Attaluri, Z. Huang, A. Belwalkar, W.V. Geertruyden, D. Gao, W. Misiolek, Evaluation of nano-porous alumina membranes for hemodialysis application, ASAIO, 55 (2009) 217-223.
[14] G.E.J. Poinern, N. Ali, D. Fawcett, Progress in nano-engineered anodic aluminum oxide membrane development, Materials, 4 (2011) 487-526.
[15] G. Meng, Y.J. Jung, A. Cao, R. Vajtai, P.M. Ajayan, Controlled fabrication of hierarchically branched nanopores, nanotubes, and nanowires, PNAS, 102 (2005) 7074-7078.
[16] D.I. Petukhov, K.S. Napolskii, A.A. Eliseev, Permeability of anodic alumina membranes with branched channels, Nanotechnology, 23 (2012) 335601.
[17] F.D.A.A. Reis, J.P. Badiali, D. di Caprio, Modeling growth of organized nanoporous structures by anodic oxidation, Langmuir, 28 (2012) 13034-13041.
[18] N. Itoh, K. Kato, T. Tsuji, M. Hongo, Preparation of a tubular anodic aluminum oxide membrane, J Mem. Sci., 117 (1996) 189-196.
[19] N. Itoh, N. Tomura, T. Tsuji, M. Hongo, Strengthened porous alumina membrane tube prepared by means of internal anodic oxidation, Microporous Mesoporous Mater., 20 (1998) 333-337.
[20] A. Belwalkar, E. Grasing, W. Van Geertruyden, Z. Huang, W.Z. Misiolek, Effect of processing parameters on pore structure and thickness of anodic aluminum oxide (AAO) tubular membranes, J Mem. Sci., 319 (2008) 192-198.
[21] S. Ichimura, T. Tsuru, S. Nakao, S. Kimura, Analysis of linear macromolecule transport through aluminum anodic oxide membranes by pore model, J Chem. Eng. Jpn, 33 (2000) 141-151.

[22] D. Mattia, F. Calabrò, Explaining High flow rate of water in carbon nanotubes via solid–liquid molecular interactions, Microfluid. Nanofluid., 13 (2012) 125-130.
[23] A. Mehta, A.L. Zydney, Permeability and selectivity analysis for ultrafiltration membranes, J Mem. Sci., 249 (2005) 245-249.
[24] D.M. Kanani, W.H. Fissell, S. Roy, A. Dubnisheva, A. Fleischman, A.L. Zydney, Permeability–selectivity analysis for ultrafiltration: Effect of pore geometry, J Mem. Sci., 349 (2010) 405-410.
[25] J. Hermia, Constant pressure blocking filtration laws - Application to power-law non-newtonian fluids, Trans. IChemE, 60 (1982) 183-187.
[26] R. van Reis, A. Zydney, Bioprocess membrane technology, J Mem. Sci., 297 (2007) 16-50.
[27] G. Bolton, D. LaCasse, R. Kuriyel, Combined models of membrane fouling: Development and application to microfiltration and ultrafiltration of biological fluids, J Mem. Sci., 277 (2006) 75-84.
[28] S. Yeu, J.D. Lunn, H.M. Rangel, D.F. Shantz, The effect of surface modifications on protein microfiltration properties of Anopore™ membranes, J Mem. Sci., 327 (2009) 108-117.
[29] I. Lee, Y. Jo, Y.-T. Kim, Y. Tak, J. Choi, Electrochemical thinning for anodic aluminum oxide and anodic titanium oxide, Bull. Korean Chem. Soc., 33 (2012) 1465-1469.
[30] D.H. Choi, P.S. Lee, W. Hwang, K.H. Lee, H.C. Park, Measurement of the pore sizes for anodic aluminum oxide (AAO), Curr. App. Phys., 6, Supplement 1 (2006) e125-e129.
[31] E. Arkhangelsky, A. Duek, V. Gitis, Maximal pore size in UF membranes, J Mem. Sci., 394–395 (2012) 89-97.
[32] P. Aimar, M. Meireles, V. Sanchez, A contribution to the translation of retention curves into pore size distributions for sieving membranes, J Mem. Sc., 54 (1990) 321-338.
[33] M.H. Simonian, Spectrophotometric Determination of protein concentration, in: Current Protocols in Food Analytical Chemistry John Wiley & Sons, Inc., 2002, pp. B1.3.1-B1.3.7.
[34] L.J. Zeman, A.L. Zydney, Microfiltration and ultrafiltration: Principles and applications, Marcel Dekker Inc., 1996.
[35] J. Oh, Porous Anodic aluminum oxide scaffolds; Formation mechanisms and applications, in: Department of Materials Science and Engineering, Massachusetts Institute of Technology, 2010.
[36] J.I. Calvo, A. Bottino, G. Capannelli, A. Hernández, Pore size distribution of ceramic UF membranes by liquid–liquid displacement porosimetry, J Mem. Sci., 310 (2008) 531-538.
[37] G. Ding, R. Yang, J. Ding, N. Yuan, Y. Zhu, Fabrication of porous anodic alumina with ultrasmall nanopores, Nanoscale Res. Lett., 5 (2010) 1257 - 1263.